Synergism between n-type WO₃ and p-type δ-FeOOH semiconductors: High interfacial contacts and enhanced photocatalysis

Lucas V.C. Lima [a], Mariandry Rodriguez [a], Victor A.A. Freitas [b], Talita E. Souza [b], Antonio E.H. Machado [c], Antonio O.T. Patrocínio [c], José D. Fabris [d], Luiz C.A. Oliveira [b], Márcio C. Pereira [a,*]

[a] *Instituto de Ciência, Engenharia e Tecnologia, Universidade Federal dos Vales do Jequitinhonha e Mucuri, 39803-371 Teófilo Otoni, MG, Brazil*
[b] *Departamento de Química, ICEx, Universidade Federal de Minas Gerais, 31270-901 Belo Horizonte, MG, Brazil*
[c] *Instituto de Química, Universidade Federal de Uberlândia, 38400-902 Uberlândia, MG, Brazil*
[d] *Universidade Federal dos Vales do Jequitinhonha e Mucuri, 39100-000 Diamantina, MG, Brazil*

ARTICLE INFO

ABSTRACT

Solar-activated p-type δ-FeOOH/n-type WO₃·H₂O photocatalysts with different tungsten contents were prepared by a facile method, even though single δ-FeOOH or WO₃·H₂O exhibits lower photocatalytic activity. The photocatalysts were extensively characterized by X-ray fluorescence spectroscopy (XRF), X-ray powder diffraction (XRD), scanning electron microscopy (SEM), ^{57}Fe Mössbauer spectroscopy, photoluminescence (PL), UV-Vis diffuse reflectance spectroscopy (DRS), Fourier transform infrared spectroscopy (FTIR), Raman spectroscopy, BET measurements and temperature programmed reduction (TPR). The photocatalytic activity was evaluated for the oxidation of rhodamine B (RhB) at different pH values. The results indicated that the photocatalytic activity of the composite was superior to that of single WO₃·H₂O or δ-FeOOH. The optimum amount of WO₃·H₂O in the composite was 60 wt.%. Based on these results, we propose that photoexcited electrons in the conduction band (CB) of WO₃·H₂O and photogenerated holes in the valence band (VB) of δ-FeOOH quickly combine, which results in the oxidation of the RhB dye by the accumulated holes in the VB of WO₃·H₂O. The total organic carbon measurements suggest that a high degree of RhB mineralization was achieved under solar light. The δ-FeOOH/WO₃·H₂O-assisted photocatalytic degradation of RhB should occur via two competitive processes (i.e., a photocatalytic and a photosensitized process). The results indicated that RhB oxidation primarily occurs via a photocatalytic process. The results from kinetic studies using radical scavengers suggest that $O_2^{\bullet-}$ and h^+ reactive species play key roles in the degradation of RhB. The results presented in this study provide new insights for the development of novel solar-light-driven photocatalysts and their potential application for harmful pollutant degradation.

© 2014 Elsevier B.V. All rights reserved.

1. Introduction

The oxidation of harmful organic substances using photocatalysts under visible light is an interesting approach for the treatment of water and wastewater because most of the widely available solar radiation can be used in the photocatalytic process [1]. However, the choice of the photocatalyst is a crucial step for efficiently degrading pollutants in water. The photocatalytic activity of semiconductors depends on several factors, such as their photoabsorption, energy levels of the conduction and valence bands, crystallinity, particle size, morphology and electron–hole recombination rate [2–4]. Among various photocatalysts, the n-type semiconductors of tungsten oxide (WO₃) and its hydrates have been extensively studied as promising materials for solar photocatalysis due to their relatively low cost, small band gap energy (2.4–2.8 eV), high oxidation power of the valence band holes, nontoxicity and stability [5–10]. However, single phase WO₃ and its hydrates typically exhibit very poor photocatalytic activity under visible light irradiation due to the fast recombination of photogenerated electrons and holes [11]. Therefore, the practical use of bare WO₃ and its hydrates as photocatalysts is limited.

To overcome the drawback of low photocatalytic efficiency due to fast electron–hole recombination in WO_3 or its hydrates, strategies based on coupling WO_3 or its hydrates and different semiconductors with matched band potentials have been developed [12–15]. The combination between WO_3 and TiO_2 particles has been extensively studied because the coupling of these two semiconductors can provide a material with improved photocatalytic activity [12,16–18]. In addition to TiO_2, other semiconductors, such as $NiWO_4$ [13], SnS_2 [14], Bi_2WO_6 [19], Fe_2O_3 [15,20], g-C_3N_4 [21,22], reduced graphene oxide [23,24], $CaFe_2O_4$ [25], $NaNbO_3$ [26] and Cu_2O [27], have been coupled with WO_3 to improve the charge separation in the resulting photocatalyst. Despite the progress that has been made, the fabrication of efficient heterojunction-based semiconductors remains a challenging task. To improve the photoactivity of semiconductors, two key factors should be addressed including (i) the design of architectures with a high interfacial area over the volume of the heterojunctions and (ii) synergistic effects between the individual heterojunctions.

Recently, a p-type semiconductor (i.e., δ-FeOOH) has attracted attention for hydrogen and oxygen evolution by water splitting and photocatalytic degradation of organic pollutants under UV or visible light irradiation [28–30]. The band gap energy of δ-FeOOH is approximately 2.2 eV [28], which enables the absorption of visible light up to 560 nm. However, the photocatalytic efficiency of single δ-FeOOH is limited due to high electron–hole recombination rates. However, if δ-FeOOH is combined with WO_3 or its hydrate ($WO_3 \cdot H_2O$), a p-n δ-FeOOH/WO_3 or δ-FeOOH/$WO_3 \cdot H_2O$ heterojunction photocatalysts may be formed. The calculated valence band (VB) and conduction band (CB) positions of WO_3 are +3.44 eV and +0.74 eV, respectively. For δ-FeOOH, the VB and CB positions are +3.18 eV and +0.98 eV, respectively, which is in agreement with previously reported values [21,30]. Therefore, photoexcited electrons on the CB of WO_3 can be transferred to the VB of δ-FeOOH, which results in a Z-scheme photocatalyst. Therefore, the holes that are photogenerated on the VB of δ-FeOOH easily combine with the photoexcited electrons on the CB of WO_3, which results in efficient charge separation that increases the photocatalytic activity.

In this paper, different p-n heterojunction composites, which have a high interfacial contact and positive synergistic effect, based on δ-FeOOH/WO_3 or δ-FeOOH/$WO_3 \cdot H_2O$ were prepared using a simple method. The photocatalytic activity was evaluated by degradation of Rhodamine B (RhB) at different pH values under UVA (λ = 365 nm) and sunlight irradiation. The prepared photocatalysts were characterized in detail by various techniques. The separation mechanism of the photogenerated electrons and holes in the photocatalysts was investigated by photoluminescence, and the main reactive species involved in the photodegradation of RhB was evaluated by using suitable scavengers. Based on the experimental results, the charge separation and RhB photodegradation mechanisms have been proposed.

2. Experimental

2.1. Preparation of samples

All of the chemical reagents were analytical grade. The synthesis of the WO_3 or $WO_3 \cdot H_2O$ particles was performed according to the procedure described by Su et al. [31]. In short, 0.5 g of $Na_2WO_4 \cdot 2H_2O$ was mixed with 0.3 g of citric acid in a beaker with 30 mL of deionized water followed by stirring for 10 min. Next, still under stirring, 6 M HCl aqueous solutions were introduced to the reaction medium until the formation of a yellow precipitate occurred. After 48 h of stirring at 120 °C, the resulting solid was separated by centrifugation at 10,000 rpm for 10 min. The solid was washed with deionized water and ethanol several times and dried under air flow at 60 °C. This sample is referred to as $WO_3 \cdot H_2O$.

The δ-FeOOH nanoparticles were prepared by stirring 50 mL of an aqueous solution containing 5.5604 g of $Fe(NH_4)_2(SO_4)_2 \cdot 6H_2O$ and 50 mL of a 2 M NaOH solution followed by rapid oxidation of $Fe(OH)_2$ using 5 mL of 30% H_2O_2 [32,33]. The precipitate turned reddish brown within a few seconds, indicating the formation of δ-FeOOH.

The δ-FeOOH/$WO_3 \cdot H_2O$ composite photocatalysts were fabricated as follows: The $WO_3 \cdot H_2O$ particles were suspended in an aqueous solution and sonicated for 30 min to obtain ultradispersed $WO_3 \cdot H_2O$. Then, 5 mL of a 2 M NaOH solution was added to the dispersion and stirred for 10 min to produce negatively charged $WO_3 \cdot H_2O$ particles. To synthesize composites with different Fe/W ratios, different quantities of the Fe^{2+} solution were added to $WO_3 \cdot H_2O$ suspension followed by addition of 5 mL of H_2O_2 (30% v/v) to produce δ-FeOOH strongly attached to the tungsten oxide surface. For convenience, the composites were labeled according to the W content (i.e., W40, W20 and W15 correspond to 40, 20 and 15 wt.% of tungsten, respectively).

2.2. Materials characterization

To determine the crystal phase composition size of the photocatalysts, XRD measurements were carried out at room temperature using a Rigaku Geigerflex diffractometer equipped with a graphite diffracted-beam monochromator. The data were collected in a 2θ range of 20° to 70° using Cu-Kα radiation and a scanning speed of 1° min^{-1}. The total Fe and W content in the samples was determined with X-ray fluorescence spectroscopy (XRF) using a Phillips PW 1480 spectrometer. Scanning electron microscopy (SEM) was carried out on a JEOL analyzer coupled to an Oxford (EDS/INCA 350) energy dispersive X-ray analyzer. ^{57}Fe Mössbauer spectra were collected in constant acceleration transmission mode with a 10 mCi^{57}Co/Rh source. The spectra of all of the samples were recorded at 298 K. The data were stored in a 1024 channel MCS memory unit and fitted using the NORMOS program. Isomer shifts were calculated relative to α-Fe. UV-Vis spectroscopy with diffuse reflectance geometry was performed with a Cary 5E spectrometer from 200 to 800 nm. $BaSO_4$ powder was used as a reference (100% transmission), and the Kubelka–Munk equation was employed to manipulate the data. Fourier transform infrared spectroscopy (FTIR) was performed using a Digilab Ex-calibur Series FTS 3000 instrument with samples diluted in KBr (1% g g^{-1}) in the spectral range of 400–4000 cm^{-1} with a resolution of 8 cm^{-1} and 32 scans. The Raman spectra were obtained with a Senterra Raman microscope spectrometer (Bruker, HR800 One Labram Jobin Yvon, λ = 633 nm). The samples were focused with a 100× lens, and the spectra were obtained using a 20 s integration time, five co-additions and 3.5 cm^{-1} resolution. To prevent heat-induced phase changes via the excitation source while the Raman spectra were being collected, we utilized a line focus that produced a line shape for the excitation source at the sample surface of 25 × 1000 μm in dimension, and the laser power was 1 mW. Surface areas were determined using the BET method with a 22 point N_2 adsorption/desorption procedure in an Autosorb 1 Quantachrome gas sorption analyzer. The temperature programmed reduction (TPR) analysis was carried out in a CHEM BET 3000 TPR using H_2 (8% in N_2) with a heating rate of 10 °C min^{-1}. Photoluminescence (PL) emission spectra were recorded on a Hitachi F-4500 type fluorescence spectrophotometer over a wavelength range of 400–700 nm with the sample placed at 45° to the incident beam.

2.3. Photocatalytic assays

The photocatalytic activity of the synthesized samples was evaluated by the photocatalytic oxidation of rhodamine B (RhB) under a 6 W UVA light (λ = 365 nm) irradiation. In short, 80 mg of

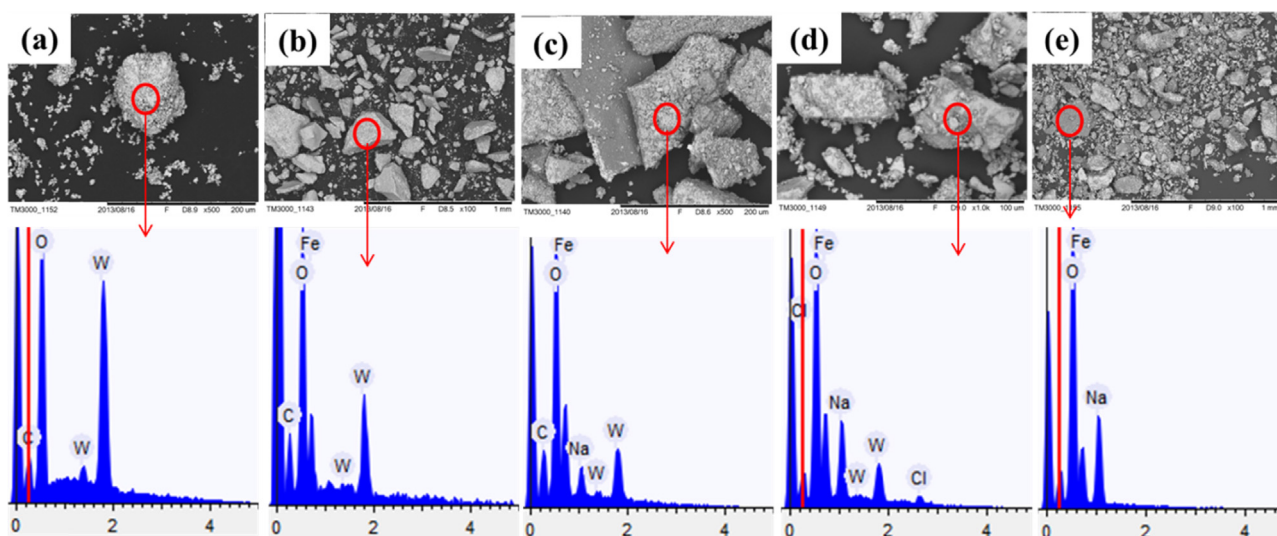**Fig. 1.** SEM images and EDX spectra of (a) $WO_3 \cdot H_2O$, (b) W40, (c) W20, (d) W15 and (e) δ-FeOOH.

the photocatalyst was added to 80 mL of a RhB aqueous solution (5 mg L^{-1}). Before irradiation, the photocatalyst was dispersed in the suspension by magnetic stirring in the dark for 90 min to achieve adsorption–desorption equilibrium between the photocatalyst and RhB. Then, the RhB suspension was irradiated with UVA light. The suspension was sampled every 30 min followed by centrifugation to separate the photocatalyst particles. Finally, the supernatants were analyzed at 554 nm using a spectrophotometer.

2.4. Evaluation of solar photocatalytic activity

The $WO_3 \cdot H_2O$, δ-FeOOH and W40 photocatalysts were evaluated for the solar degradation of RhB. The solar irradiation intensity was measured every 30 min using a Solar Light PMA 2100 radiometer. All of the experiments were performed on sunny days (~1030 W/m^2) between 11:00 and 16:00 h when the solar intensity fluctuations were minimal. The accumulated dose of solar radiation (kJ) incident to the photoreactor was calculated from the light irradiance. The photocatalytic tests were carried out by adding 200 mg of the catalyst to the reactor containing 2000 mL of an aqueous solution of RhB (5 mg L^{-1}). The pH of the solution was adjusted to 9 using 0.2 mol L^{-1} NaOH. The experiments were conducted outside using solar radiation. During irradiation, stirring was employed to maintain a homogeneous suspension. At regular intervals, samples were withdrawn and analyzed at 554 nm using a spectrophotometer.

The mineralization of RhB was quantified by combustion catalytic oxidation using a total organic carbon analyzer (TOC-V, Shimadzu).

2.5. Detection of reactive species

The evaluation the reactive species formed during the photocatalytic degradation of RhB was based on the use of different scavenger molecules introduced to the reaction medium prior to the addition of the photocatalysts. The dosage of these scavengers was 10 mM.

3. Results and discussion

3.1. Characterization of the photocatalysts

Fig. 1 shows the SEM images and the corresponding EDX spectra of the particles prepared with various compositions of Fe and W.

When using 0 wt.% Fe (only $WO_3 \cdot H_2O$), an agglomeration of small particles with an undefined shape were produced (Fig. 1a). Samples W40 (Fig. 1b), W15 (Fig. 1d) and δ-FeOOH (Fig. 1e) are very similar, and they exhibit irregular shapes with inhomogeneous grain sizes. Sample W20 (Fig. 1c) possesses a 2D plate-like structure of varying sizes. The EDX spectrum of $WO_3 \cdot H_2O$ (Fig. 1a) contains signals belonging to W and O with an O/W atomic ratio of approximately 4, which is consistent with the formula $WO_3 \cdot H_2O$. For composites W40, W20 and W15, the Fe/W atomic ratio is equal to 2.5, 6.3 and 7.7, respectively, which confirms the nominal amount of Fe employed in the synthesis procedure. The EDX spectrum of δ-FeOOH contains signals corresponding to Fe and O with an O/Fe atomic ratio of 2/1, which is close to the formula FeOOH. The appearance of an EDX signal corresponding to sodium ions in the spectra of W20, W15 and δ-FeOOH is due to the use of the 2 M NaOH solution for the precipitation of δ-FeOOH. Na$^+$ ions remain in these samples even after successive washings with deionized water.

Fig. 2 shows the XRD patterns of photocatalysts with different amounts of Fe and W. The sample with 0 wt.% Fe consists of a single phase of orthorhombic $WO_3 \cdot H_2O$ (JCPDS 18-1418). Upon addition of Fe, the XRD patterns of all of the samples indicated the formation of hexagonal δ-FeOOH, which was identified from its (1 0 0),
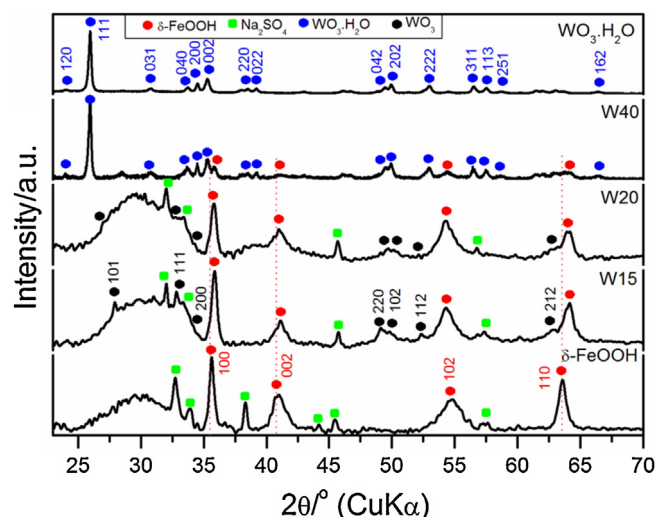

Fig. 2. Powder XRD patterns of the photocatalysts.

Table 1
Elemental chemical composition obtained by XRF.

Sample	Elemental analysis (wt.%)		
	Fe	W	Na
$WO_3·H_2O$	–	73.3	–
W40	25.2	41.2	–
W20	41.0	22.1	2.3
W15	39.5	14.6	6.2
δ-FeOOH	44.2	–	9.8

Table 2
Hyperfine field parameters of the Mössbauer spectra recorded at room temperature. δ = isomer shift, Δ = quadrupole splitting, $2\varepsilon_Q$ = quadrupole shift, B_{hf} = magnetic hyperfine field, RA = relative subspectral area.

Sample	δ (mm s^{-1})	Δ, $2\varepsilon_Q$ (mm s^{-1})	B_{hf} (T)	RA (%)
δ-FeOOH	0.40	0.63	–	10
	0.37	−0.15	49.8*	90
W15	0.38	0.64	–	13
	0.36	−0.18	49.0*	87
W20	0.38	0.62	–	11
	0.37	−0.19	49.8*	89
W40	0.40	0.64	–	15
	0.37	−0.22	49.8*	85

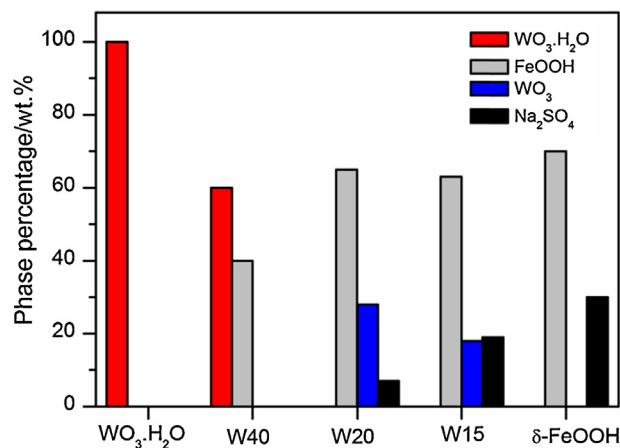* Parameter fixed during the fitting procedure.

Fig. 3. Percentage of phases in the photocatalysts.

(0 0 2), (1 0 2) and (1 1 0) diffraction planes according to JCPDS 13-87. In addition to δ-FeOOH, composite W40 exhibited diffraction peaks that correspond to $WO_3·H_2O$, and samples W20 and W15 consist of WO_3 (JCPDS 5-388), which confirms the formation of δ-FeOOH/$WO_3·H_2O$ and δ-FeOOH/WO_3. It is should be noted that when δ-FeOOH is coupled with WO_3 or $WO_3·H_2O$, the characteristic peaks of δ-FeOOH are shifted to a higher diffraction angle by 0.4° compared to the XRD pattern of bare δ-FeOOH, which suggests a strong interaction between δ-FeOOH and WO_3 or $WO_3·H_2O$. The XRD patterns of samples W20, W15 and δ-FeOOH indicated that the sodium observed in the EDX spectra of these samples was due to residual Na_2SO_4 that was formed in the synthesis procedure.

The quantitative chemical composition of the prepared samples was analyzed by XRF, and the results are shown in Table 1. Based on XRF elemental analysis and the XRD data, we determined the percentage of each phase in the prepared photocatalysts (Fig. 3). Samples δ-FeOOH, W20 and W15 contain a similar amount of δ-FeOOH (63–70 wt.%), and the amount of WO_3 in these samples was

0, 28 and 18 wt.%, respectively. However, W40 was composed of 60 wt.% $WO_3·H_2O$ and 40 wt.% δ-FeOOH.

To better understand the distribution of iron in the δ-FeOOH structure, Mössbauer spectra were collected at 298 K. The spectra of the photocatalysts (Fig. 4a) were fitted using a magnetic hyperfine field distribution due to the inhomogeneous particle size of δ-FeOOH. The fitted parameters are summarized in Table 2. The two main magnetically split components (Fig. 4b) correspond to iron in octahedral sites in the δ-FeOOH structure [34,35]. It is interesting to observe that an increase in the quadrupole shift ($2\varepsilon_Q$) is directly proportional to the W content, which indicates a high distortion in the δ-FeOOH structure due to its strong interaction with the WO_3 or $WO_3·H_2O$ particles in the composites. In addition to these two main magnetically split components, the spectra of all of the photocatalysts exhibit an Fe^{3+} doublet due to the very small particles of δ-FeOOH. In addition, the higher relative subspectral area of the Fe^{3+} doublet in sample W40 indicates that the δ-FeOOH nanoparticles are better dispersed than in the other samples.

The FTIR spectra of the photocatalysts are shown in Fig. 5a. The spectrum of $WO_3·H_2O$ contains a sharp IR band at 950 cm^{-1} and a very strong and broad band at 670 cm^{-1}, which corresponds to the ν(W=O) and ν(O–W–O) vibrations, respectively [36]. For $WO_3·H_2O$, the W=O bond peak, which is typical of non-bridging O, is caused by structural water molecules. One of the axial O positions in the octahedron can be occupied by a structural water molecule. This O is associated with a single bond, and the opposite axial O forms a strong W=O terminal double bond. In comparison to the single $WO_3·H_2O$, composites W40, W20 and W15 exhibit a slightly shifted band from 950 cm^{-1} to 944, 938 and 935 cm^{-1}, respectively, due to the strong interaction between the WO_3 matrix and the δ-FeOOH nanoparticles. The FTIR spectrum of δ-FeOOH contains weak

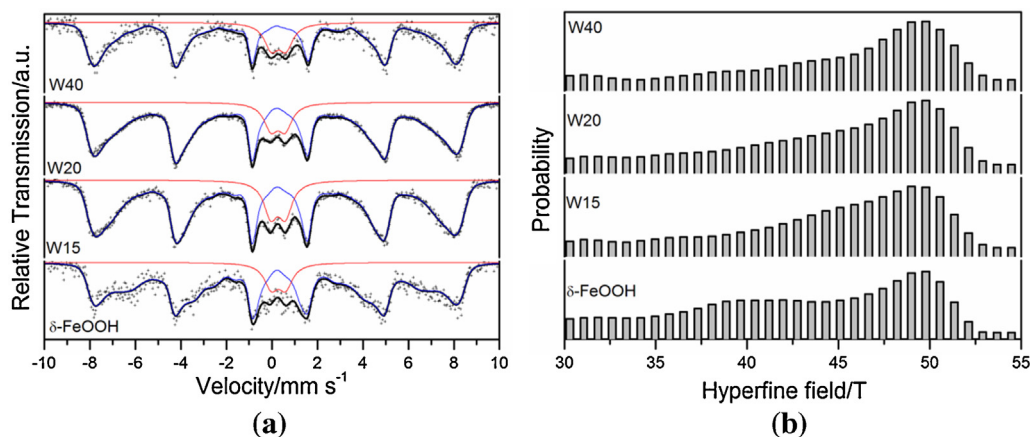**Fig. 4.** (a) ^{57}Fe Mössbauer spectra of the photocatalysts collected at 298 K and (b) hyperfine field distribution for Fe^{3+} in the δ-FeOOH.
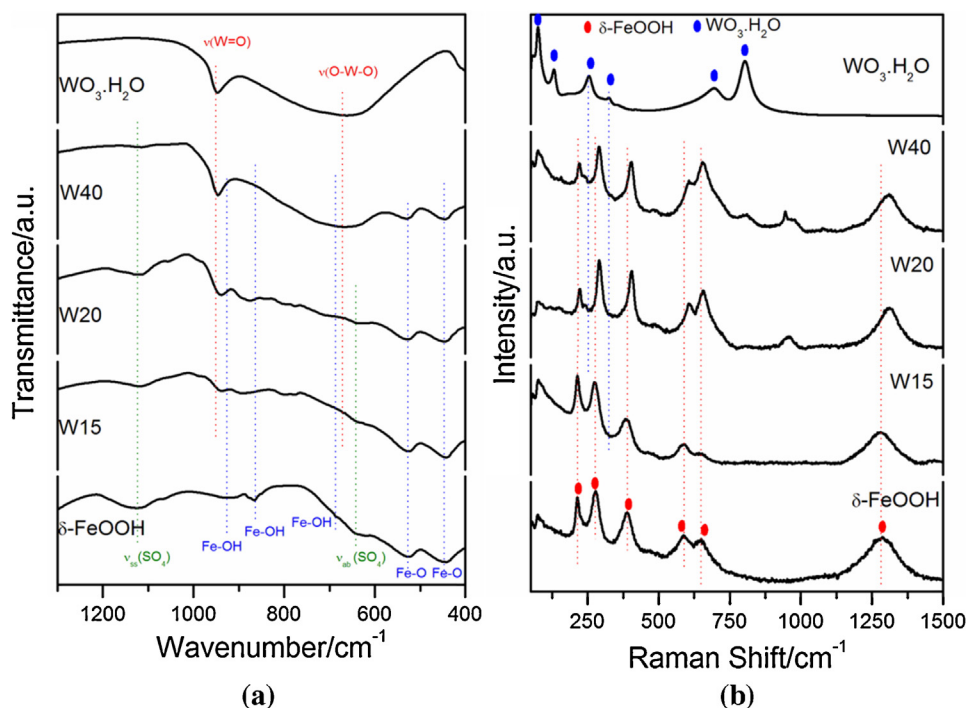
Fig. 5. (a) FTIR spectra of the photocatalysts and (b) Raman spectra of the photocatalysts.

broad bands at 926, 862 and 686 cm^{-1}, which were assigned to the Fe—OH bending modes. The IR bands at 446 and 526 cm^{-1} were assigned to the vibrations of the Fe—O bond in the δ-FeOOH structure [37]. Interestingly, the band at 862 cm^{-1} for δ-FeOOH shifted to 889 and 885 cm^{-1} in W15 and W20, respectively, which indicates the interaction between δ-FeOOH and WO$_3$. The band at 1123 and 641 cm^{-1} corresponding to the vibrational frequencies of symmetric and asymmetric SO$_4$ are due to SO$_4^{2-}$ ions arising from residual Na$_2$SO$_4$ in these samples [38], which was confirmed by XRD.

The strong interaction between δ-FeOOH and WO$_3$ or WO$_3$·H$_2$O was also confirmed by the Raman spectral analysis (Fig. 5b). The Raman spectrum of WO$_3$·H$_2$O exhibits six distinct peaks located at 75, 131, 254, 325, 699 and 804 cm^{-1} [36], and the Raman spectrum of δ-FeOOH exhibited peaks located at 216, 276, 390, 589, 652 and 1284 cm^{-1} [39,40]. The Raman spectra of the composites were dominated by δ-FeOOH bands suggesting that δ-FeOOH covers the WO$_3$ or WO$_3$·H$_2$O surfaces, which was confirmed by the SEM images shown in Fig. 1. In addition, the band at 254 cm^{-1} for WO$_3$·H$_2$O is slightly shifted to 245 and 241 cm^{-1} in composites W40 and W20, respectively, and the bands corresponding to δ-FeOOH are shifted in the composites. For example, the band at 276 cm^{-1} was shifted to 281, 293 and 293 in composites W15, W20 and W40, respectively. The band related to δ-FeOOH at 390 cm^{-1} was shifted to 395, 406 and 406 cm^{-1} in the same sequence of composites, and the band at 1284 cm^{-1} was shifted to 1293, 1315 and 1320 cm^{-1} in the same sequence of composites. In addition to these changes, the bands at 589 and 652 cm^{-1} were also shifted in the composites with variations in their relative intensities. The relative intensity of I_{589} was higher than that at I_{652} in δ-FeOOH and W15. However, in composites W40 and W20, the opposite was observed (i.e., I_{652} is higher than I_{589}). This result clearly suggests a strong interaction between δ-FeOOH and WO$_3$, and therefore, the as-prepared photocatalysts are composites instead of simple mixtures.

The composites were also characterized using TPR because this technique allows us to estimate the reducibility of iron species [41], which depends on the interaction between the iron in δ-FeOOH and WO$_3$ particles. Therefore, the TPR profiles of the

photocatalysts can provide information on the interaction of these species in the composite. Strongly attached iron oxide in a matrix reduces slower compared to a simple mixture. The H$_2$-TPR profile of δ-FeOOH (Fig. 6) exhibits three reduction peaks centered at 520, 710 and 759 °C, which correspond to the following phase transitions: (i) reduction δ-FeOOH into magnetite (Fe$_3$O$_4$), reduction of magnetite into wüstite (FeO) and (iii) reduction of wüstite into metallic iron (Fe), respectively. The H$_2$-TPR profile of WO$_3$·H$_2$O contained two peaks with maxima at 675 and 756 °C. These peaks might be assigned to the stepwise reduction of WO$_3$(VI) → W$_{20}$O$_{58}$ (V, VI) → WO$_2$(IV) [42]. As shown in Fig. 6, the H$_2$-TPR profiles of W40 contain two reduction peaks at 539 and 694 °C due to the conversion of δ-FeOOH in FeO (δ-FeOOH → Fe$_3$O$_4$ → FeO). For W20, the corresponding reduction peaks were centered at 576 and 800 °C, and for W15, the reduction peaks were located at 564 and 800 °C. It should be noted that the first reduction in the composites (δ-FeOOH → Fe$_3$O$_4$) was shifted from 520 °C in the single δ-FeOOH
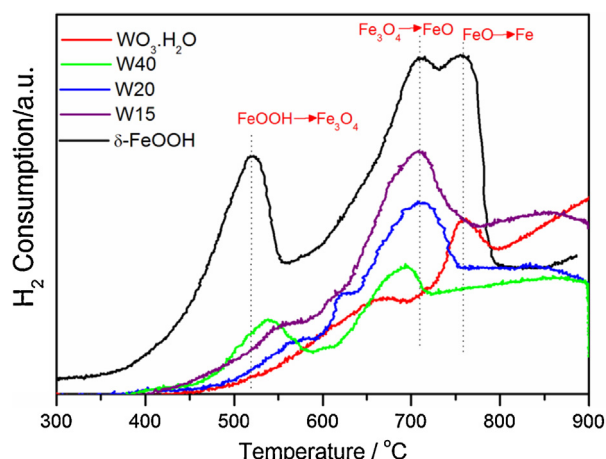

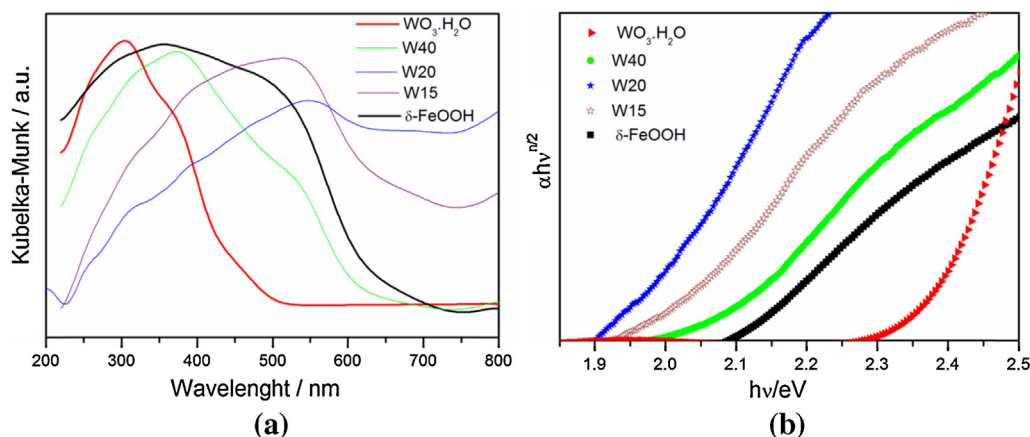**Fig. 6.** H$_2$-TPR profiles of the photocatalysts.

Fig. 7. (a) UV-Vis diffuse reflectance spectra of the photocatalysts and (b) band gap energies of the photocatalysts.

to 539, 576 and 564 °C in W40, W20 and W15, respectively. This increase in the reduction temperature suggests that δ-FeOOH is strongly attached to the WO_3 or $WO_3 \cdot H_2O$ surfaces. These results are in agreement with the XRD, Raman and FTIR data.

To investigate the electronic structure of the as-prepared photocatalysts, UV–vis diffuse reflectance spectra were recorded (Fig. 7). From Fig. 7a, δ-FeOOH shows absorption features from the UV to the visible region up to 600 nm, which correspond to the intrinsic band gap of δ-FeOOH (2.04 eV, Fig. 7b). The indirect band gap energy estimated for $WO_3 \cdot H_2O$ was 2.34 eV, which suggests that $WO_3 \cdot H_2O$ absorbs light from the UV region to 540 nm. In comparison to pure $WO_3 \cdot H_2O$, the absorption wavelength region of W40, W20 and W15 was extended toward the visible light region, and a stronger absorption in the visible region at wavelengths longer than 400 nm was observed. The red shift and absorbance intensity in the visible region were simultaneously improved as the amount of δ-FeOOH increased, which results in efficient solar light-driven photocatalysis. These results may be due to the strong interaction between δ-FeOOH and WO_3 in the composite photocatalysts. The band gap energies for the composites were calculated using the following equation:

$$\alpha h\nu = A(h\nu - E_g)^{n/2} \tag{1}$$

where α, h, ν, A and E_g are the absorption coefficient, Planck's constant, light frequency, proportionality constant and band gap energy, respectively. In addition, n is the transition order in a semiconductor (i.e., $n = 1$ for direct transition and $n = 4$ for indirect transition). The values of n for δ-FeOOH and WO_3 are 1 and 4, respectively. By applying this equation, the band gaps of W40, W20 and W15 are 2.18, 1.50 and 1.82 eV, respectively.

The PL spectra of the photocatalysts are shown in Fig. 8. $WO_3 \cdot H_2O$ and δ-FeOOH do not exhibit any emission signals at room temperature, which is most likely due to the electron–hole recombination in these materials being much faster than the radiative decay. However, when $WO_3 \cdot H_2O$ is combined with δ-FeOOH, the rate of electron and hole recombination should decrease, and a weak emission peak at 600 nm was observed in the PL spectra of W15, W20 and W40, which was more pronounced in the last two photocatalysts. This result suggests more effective charge transfer in these materials. This emission is related to recombination of the photoexcited electron–hole pair in δ-FeOOH due to direct transfer of electrons from $WO_3 \cdot H_2O$ CB to δ-FeOOH VB, which produces an efficient scheme for charge separation in $WO_3 \cdot H_2O$. In this scheme, the holes in the valence band of $WO_3 \cdot H_2O$ can effectively promote the oxidation of RhB.

The N_2 adsorption–desorption curves for the photocatalysts are shown in Fig. 9a, and the corresponding pore size distribution is
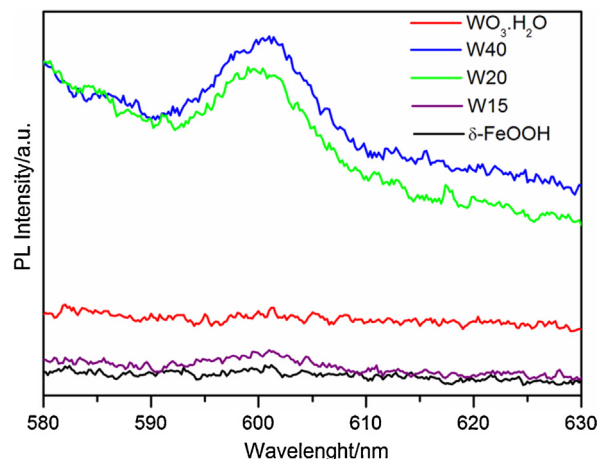

Fig. 8. PL spectra of the photocatalysts (excitation wavelength = 400 nm).

shown in Fig. 9b. The N_2 adsorption–desorption curves for all of the photocatalysts exhibit a type II isotherm, which is typical of mesoporous materials (Fig. 9b), with a small type H4 hysteresis loop. The BET surface area of $WO_3 \cdot H_2O$, W40, W20, W15 and δ-FeOOH was 42, 38, 13, 46 and 59 $m^2\,g^{-1}$, respectively.

3.2. Photocatalytic assays

The photocatalytic activities of the prepared materials were evaluated via the degradation of RhB. At a pH of 7, the adsorption by the photocatalysts in the absence of irradiation results in removal of 19, 6, 39, 9 and 3% of the RhB from the solution by adsorption using the $WO_3 \cdot H_2O$, W40, W20, W15 and δ-FeOOH photocatalysts, respectively (Fig. 10a). The removal of RhB by photocatalysis using UVA light irradiation reached 31, 21, 40, 17 and 19% in the presence of $WO_3 \cdot H_2O$, W40, W20, W15 and δ-FeOOH, respectively, after 3.5 h. However, the mechanical mixture of δ-FeOOH + $WO_3 \cdot H_2O$ removed only 12% of the RhB, which indicated that contact between δ-FeOOH and $WO_3 \cdot H_2O$ is essential for obtaining an active system.

The quantitative aspects of the reaction kinetics related to RhB photodegradation were studied according to the Langmuir-Hinshelwood kinetic model, which can be expressed by the following apparent pseudo first-order kinetics equation [43]:

$$-\ln\frac{C}{C_0} = k_{app}t \tag{2}$$

where k_{app} is the apparent pseudo first-order rate constant (min^{-1}), C is the RhB concentration in the aqueous solution at time t $(mg\,L^{-1})$
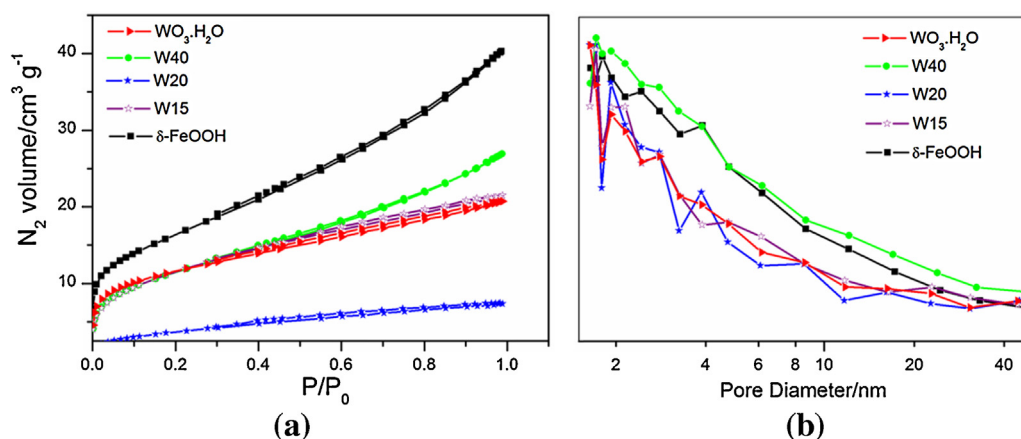
Fig. 9. (a) Nitrogen adsorption–desorption isotherms and (b) pore size distribution in the photocatalysts.

and C_0 is the initial RhB concentration (mg L^{-1}). The k_{app} of the photocatalysts (i.e., WO$_3$·H$_2$O, W40, W20, W15 and δ-FeOOH) normalized by their specific areas, were 2.17×10^{-5}, 2.37×10^{-5}, 3.30×10^{-4}, 1.87×10^{-5} and 1.54×10^{-5} min^{-1} m^{-2} g, respectively.

To better understand the effect of pH on the photocatalytic activity of the prepared materials, RhB photodegradation experiments at a pH of 4 and 9 were also performed. At a pH of 4 (Fig. 10b), the adsorption of RhB on the photocatalyst surfaces was increased substantially compared to the RhB adsorption results at pH 7. Photocatalysts WO$_3$·H$_2$O, W40, W20, W15 and δ-FeOOH removed 17, 45, 82, 75 and 15%, respectively, of RhB after 1.5 h of adsorption in the dark. Upon 3.5 h of reaction under black light irradiation, the decolorization of RhB reached 19, 56, 86, 84 and 18% for WO$_3$·H$_2$O, W40, W20, W15 and δ-FeOOH, respectively. However, the RhB color removal was primarily due to the adsorption process. Although the low photocatalytic activity of WO$_3$·H$_2$O, W40, W20, W15 and δ-FeOOH indicated by the small variation in the dye concentration during the photolysis and also by their rate constants (i.e., 7.62×10^{-6}, 4.71×10^{-5}, 9.69×10^{-5}, 6.33×10^{-5} and 2.88×10^{-6} min^{-1} m^{-2} g, respectively), at a pH of 4, the junction between WO$_3$ and δ-FeOOH is essential for achieving a high percentage of RhB color removal, as shown in Fig. 10b.

At a pH of 9 (Fig. 10c), the dye removal in dark conditions was 3, 22, 14, 6 and 7% due to adsorption of RhB on WO$_3$·H$_2$O, W40, W20, W15 and δ-FeOOH, respectively. Interestingly, under UVA light irradiation, the photocatalytic effect of the prepared materials was more easily observed. The photolysis process contributed to 25% of the color removal of RhB. Nevertheless, RhB is not a sensitizer for δ-FeOOH because it does not exhibit any photocatalytic activity at a pH of 9. However, after a 3.5 h reaction, the photodegradation of RhB was 44, 69, 49 and 25% in the presence of the WO$_3$·H$_2$O, W40, W20 and W15 photocatalysts, respectively. It can be noted that the higher photocatalytic activity was due to sample W40, which has smaller surface area than their single components. It suggests that the strong interaction between δ-FeOOH and WO$_3$·H$_2$O in the composites is more important for the photocatalytic oxidation of RhB than the surface area.

The rate constants of the RhB degradation in the presence of the photocatalysts changed after an 1.5 h of reaction. Therefore, we suggest that the photodegradation of RhB in the presence of our photocatalysts should occur by two competitive processes: **(1)** photosensitization and **(2)** photocatalytic process. During the first 90 min of the reaction, the rate reaction is driven by process **(1)**, and after this time, process **(2)** is primarily responsible for the reaction rate. The rate constants obtained in process **(1)** for the degradation induced in the presence of WO$_3$·H$_2$O, W40, W20 and W15 were 5.54×10^{-3}, 1.30×10^{-3}, 2.18×10^{-3} and

2.7×10^{-3} min^{-1}, respectively. For process (2), the rate constants were 1.91×10^{-3}, 6.08×10^{-3}, 3.22×10^{-3} and 4.45×10^{-3} min^{-1} for the same sequence of photocatalysts.

3.3. Reactive species

The reactive species in the degradation of RhB in the presence of W40 were investigated. It is generally accepted that organic compounds can be degraded via photocatalytic oxidation by different species, such as holes (h$^+$), hydroxyl (•OH) and/or superoxide radicals (O$_2^{•-}$) [44–46]. Therefore, several scavengers, such as ammonium oxalate (AO), isopropanol (IPA) and benzoquinone (BQ), were employed to trap h$^+$, •OH and O$_2^{•-}$, respectively [44–46]. By adding different scavengers to the reaction media to remove the corresponding reactive species, the role of different reactive species in the photocatalytic process can be evaluated based on changes in the photocatalytic efficiency.

Fig. 11 shows the photocatalytic activity of W40 in the degradation of RhB under different conditions. Without the addition of scavengers, the decolorization of RhB was 68% after 210 min of irradiation. By adding IPA to suppress •OH, the decolorization efficiency of RhB was not significantly affected, which indicated that the •OH is not an important reactive species in this system. However, when AO was used as a hole-trap, the photodegradation of RhB decreased to 13%, indicating that the photogenerated holes are very important to the photocatalytic process on the W40 composite. In the presence of BQ, the decolorization efficiency substantially decreased to 6%. Based on these results, it is evident that O$_2^{•-}$ and h$^+$ are the main reactive species in the photocatalytic reaction mediated by W40.

3.4. Possible RhB photodegradation mechanism

It is well known that RhB can absorb visible light in the range of 460–600 nm. In addition, the calculated band gap energies for WO$_3$·H$_2$O and δ-FeOOH were 2.34 and 2.04 eV, respectively. Therefore, RhB, WO$_3$·H$_2$O and δ-FeOOH can be excited by UVA light, and RhB can be degraded via a photosensitized oxidation mechanism, which was confirmed in the photocatalysis experiments. The schematic diagram of RhB photodegradation using δ-FeOOH/WO$_3$·H$_2$O is shown in Fig. 12. First, RhB absorbs the incident photons through a $\pi \rightarrow \pi^*$ transition resulting in an RhB* excited state, which is able to inject electrons into the CB of WO$_3$·H$_2$O. However, the photoelectrons in the CB of this photocatalyst cannot be captured by O$_2$, which limits the effective degradation of RhB and its subsequent mineralization. In fact, the photodegradation of RhB induced by the electronically excited dye is very slow compared to the photocatalytic process mediated by
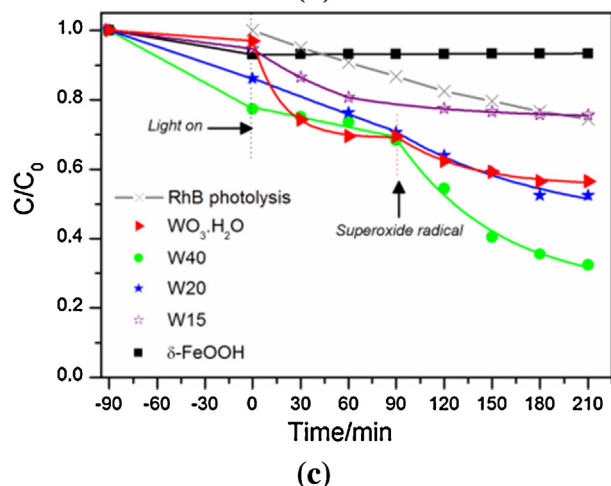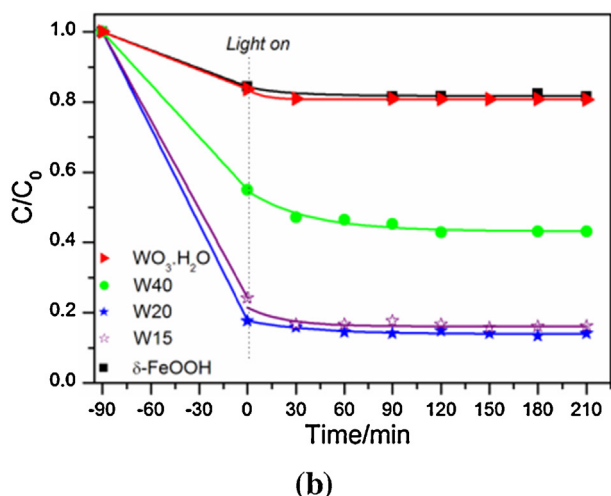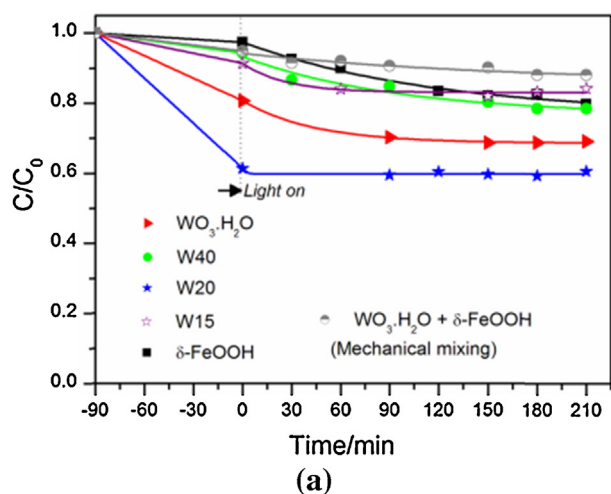
(a)

(b)

(c)

Fig. 10. Photocatalytic degradation of RhB induced by the photocatalysts under UVA light irradiation and different pH values: (a) pH 7, (b) pH 4 and (c) pH 9.

δ-FeOOH/WO$_3$·H$_2$O (W40). As mentioned above, only 25% of the RhB was oxidized by photosensitization.

In the photocatalytic process, the promotion of an electron from the VB to the CB of a semiconductor generates active sites (holes) for RhB oxidation. Based on the band structures of δ-FeOOH and WO$_3$·H$_2$O and the effects of the scavengers, a pathway for the photocatalytic process based on the W40 photocatalyst has been proposed. As shown in Fig. 12, for the δ-FeOOH/WO$_3$·H$_2$O system,
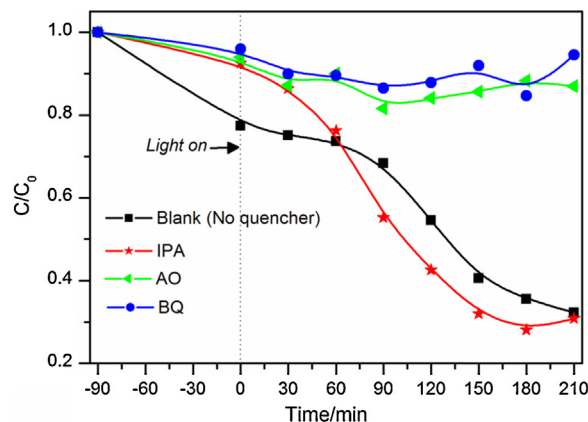

Fig. 11. Photocatalytic degradation of RhB induced by the W40 photocatalyst under different conditions with exposure to UVA light: IPA = isopropanol; AO = ammonium oxalate and BQ = benzoquinone.

both δ-FeOOH and WO$_3$·H$_2$O can be simultaneously excited by light to form e$^-$/h$^+$ pairs. The photoinduced electrons can be transferred from the bottom of the CB of WO$_3$·H$_2$O to the valence band of δ-FeOOH, as suggested by the photoluminescence data. These accumulated electrons in the CB of δ-FeOOH cannot reduce O$_2$ to yield O$_2^{\bullet-}$ because the CB edge potential of δ-FeOOH (0.82 eV vs. NHE, at pH 9) is more positive than the standard redox potential E$^\theta$ (O$_{2/}$O$_2^{\bullet-}$) (−0.86 eV NHE, at pH 9). In fact, the photocatalytic efficiencies in the presence of dissolved oxygen and under anoxic conditions (data not shown) were very similar, which indicated that O$_2$ is not important for this photocatalytic system. The more positive VB position of WO$_3$·H$_2$O (2.97 eV vs. NHE, at pH 9) suggests that the oxidation of $^-$OH or H$_2$O to $^\bullet$OH or $^\bullet$OOH by h$^+$ is favored. However, under the experimental conditions, the results indicated that $^\bullet$OH radicals are not important in the δ-FeOOH/WO$_3$·H$_2$O system. In addition, our experimental results strongly suggest that RhB is photocatalytically degraded by O$_2^{\bullet-}$ or directly by h$^+$. According to Tizaoui et al. [47], once the $^\bullet$OOH radicals are formed, an acid/base equilibrium with O$_2^{\bullet-}$ develops in aqueous medium (Eq. 3):

$$^\bullet OOH \rightleftharpoons O_2^{\bullet-} + H^+ \tag{3}$$

Because the pKa of this equilibrium is 4.88 [47] and the pH used in the RhB photodegradation was 9, the superoxide form is dominant. Therefore, we proposed that O$_2^{\bullet-}$ trapped by the scavenger is derived from the equilibrium shown in Eq. (3) instead of from O$_2$ reduction.
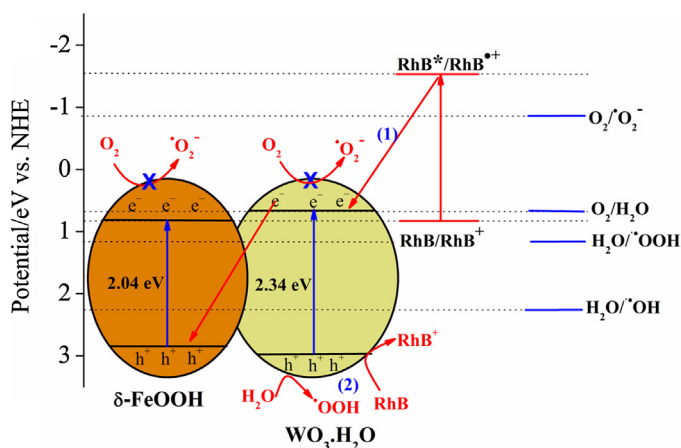

Fig. 12. Schematic diagram of photoexcited electron–hole separation process and the proposed mechanism for RhB degradation.
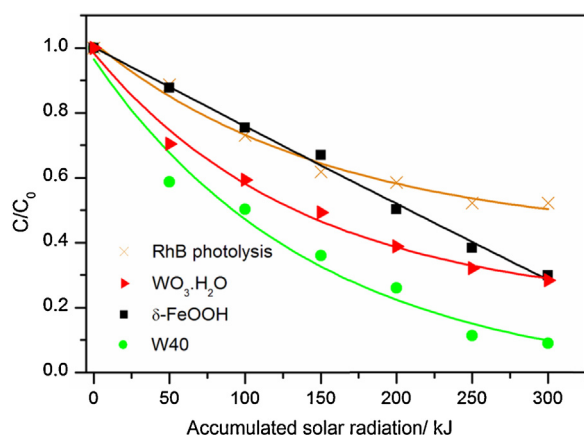
Fig. 13. Photocatalytic degradation of RhB induced by δ-FeOOH, WO₃·H₂O and W40 under solar irradiation at pH 9.

In summary, the δ-FeOOH/WO₃·H₂O-assisted photodegradation of RhB may occur via two main processes including a photocatalytic and a dye-photosensitized process. Both the photocatalytic and the photosensitized process most likely occur concurrently. However, the photocatalytic process is the predominant process due to the existence of a heterojunction between δ-FeOOH and WO₃·H₂O.

3.5. Photodegradation of RhB by sunlight-activated photocatalysis

The photodegradation efficiency of WO₃·H₂O, δ-FeOOH and W40 was evaluated under solar light irradiation based on the degradation percent estimated by photometric measurements and the mineralization of an initial concentration of $5\,mg\,L^{-1}$ RhB in an aqueous medium at pH 9 with a photocatalyst loading of $100\,mg\,L^{-1}$. A solution with a pH of 9 was chosen for the photocatalytic experiments based on previous results that demonstrated that RhB degradation occurs rapidly under alkaline conditions.

In RhB photocatalytic degradation induced by sunlight in the absence of a catalyst (Fig. 13), approximately 48% of the RhB color was removed when the accumulated solar UVA radiation reached 300 kJ. In the presence of WO₃·H₂O, δ-FeOOH and W40, the RhB color removal was 71, 70 and 92%, respectively. The results suggest that the photocatalytic process is effective for RhB color removal and therefore its oxidation. The best result was observed when W40 was used, which is most likely due the intimate contact between δ-FeOOH and WO₃·H₂O that leads to efficient charge separation in the photocatalyst.

TOC measurements were also performed to evaluate the photocatalytic ability of the photocatalysts. In the presence of W40, 78% of the RhB was mineralized after 120 min of irradiation (300 kJ), and only 17, 28 and 24% of the DOC (dissolved organic carbon) removal was converted using photolysis, WO₃·H₂O and δ-FeOOH, respectively. These data suggest that the association between WO₃·H₂O and δ-FeOOH is fundamental for obtaining high levels of mineralization of the organic matter under solar light.

4. Conclusions

The δ-FeOOH/WO₃·H₂O p–n heterojunctions with different WO₃ contents were prepared using a simple method. δ-FeOOH/WO₃·H₂O exhibited enhanced photocatalytic activity compared to single WO₃·H₂O or δ-FeOOH in RhB degradation under UVA light and solar light irradiation. The efficient separation of electrons and holes that originated from the formation of δ-FeOOH/WO₃·H₂O heterojunctions was essential for achieving the photocatalytic activity and mineralization compared to single WO₃·H₂O or δ-FeOOH. $O_2^{\bullet-}$ and h⁺ play a major role in RhB degradation, and the role of •OH is negligible. It is conceivable that the synergism between δ-FeOOH and WO₃ or its hydrate may stimulate application in other fields, such as water splitting and photoelectrochemical cells.

Acknowledgments

References

[1] S. Ahmed, M.G. Rasul, W.N. Martens, R. Brown, M.A. Hashib, Water Air Soil Poll. 215 (2011) 3–29.
[2] N. Wu, J. Wang, D.N. Tafen, H. Wang, J.G. Zheng, J.P. Lewis, X. Liu, S.S. Leonard, A. Manivannan, J. Am. Chem. Soc. 132 (2010) 6679–6685.
[3] A.M. Smith, S. Nie, Accounts Chem. Res. 43 (2009) 190–200.
[4] H. Yu, H. Irie, K. Hashimoto, J. Am. Chem. Soc. 132 (2010) 6898–6899.
[5] P. Wang, B. Huang, X. Qin, X. Zhang, Y. Dai, M.H. Whangbo, Inorg. Chem. 48 (2009) 10697–10702.
[6] H. Zheng, J.Z. Ou, M.S. Strano, R.B. Kaner, A. Mitchell, K. Kalantar-zadeh, Adv. Funct. Mater. 21 (2011) 2175–2196.
[7] A.B.D. Nandiyanto, O. Arutanti, T. Ogi, F. Iskandar, T.O. Kim, K. Okuyama, Chem. Eng. J. 101 (2013) 523–532.
[8] X. Wang, X. Meng, M. Zhong, F. Wu, J. Li, Appl. Surf. Sci. 282 (2013) 826–831.
[9] J. Shi, G. Hu, R. Cong, H. Bu, N. Dai, New J. Chem. 37 (2013) 1538–1544.
[10] Q. Zeng, Y. Zhao, J. Zhao, X. Hao, Y. Lu, J. Guo, Y. Song, F. Gao, Z. Huang, Cryst. Res. Technol. 48 (2013) 334–343.
[11] J. Cao, B. Luo, H. Lin, B.Y. Xu, S.F. Chen, Appl. Catal. B: Environ. 111 (2012) 288–296.
[12] I.A. Castro, W. Avansi Jr., C. Ribeiro, Cryst. Eng. Comm. 16 (2014) 1514–1524.
[13] M.M. Mohamed, S.A. Ahmed, K.S. Khairou, Appl. Catal. B—Environ. 150–151 (2014) 63–73.
[14] J. Li, X. Du, L. Yao, Y. Zhang, Mater. Lett. 121 (2014) 44–46.
[15] D. Bi, Y. Xu, J. Mol. Catal. A—Chem. 367 (2013) 103–107.
[16] O. Arutanti, A.B.D. Nandiyanto, T. Ogi, F. Iskandar, T.O. Kim, K. Okuyama, J. Alloy Compd. 591 (2014) 121–126.
[17] K.I. Liu, Y.C. Hsueh, H.S. Chen, T.P. Pergn, J. Mater. Chem. A 2 (2014) 5387–5393.
[18] F. Riboni, L.G. Bettini, D.W. Bahnemann, E. Selli, Catal. Today 209 (2013) 28–34.
[19] G.H. He, G.L. He, A.J. Li, X. Li, X.J. Wang, Y.P. Fang, Y.H. Xu, J. Mater. Chem. A 385 (2014) 106–111.
[20] S. Bai, K. Zhang, J. Sun, R. Luo, D. Li, A. Chen, Cryst. Eng. Comm. 16 (2014) 3289–3295.
[21] S. Chen, Y. Hu, S. Meng, X. Fu, Appl. Catal., B—Environ. 150–151 (2014) 564–573.
[22] Z. Jin, N. Murakami, T. Tsubota, T. Ohno, Appl. Catal., B—Environ. 150–151 (2014) 479–485.
[23] B. Chai, J. Li, Q. Xu, K. Dai, Mater. Lett. 120 (2014) 177–181.
[24] H. Huang, Z. Yue, G. Li, X. Wang, J. Huang, Y. Du, P. Yang, J. Mater. Chem. A 1 (2013) 15110–15116.
[25] M. Miyauchi, Y. Nukui, D. Atarashi, E. Sakai, ACS Appl. Mater. Interfaces 5 (2013) 9770–9776.
[26] C. Shifu, J. Lei, T. Wenming, F. Xianliang, Dalton Trans. 42 (2013) 10759–10768.
[27] S. Wei, Y. Ma, Y. Chen, L. Liu, Y. Liu, Z. Shao, J. Hazard. Mater. 194 (2011) 243–249.
[28] M.C. Pereira, E.M. Garcia, A.C. Silva, E. Lorençon, J.D. Ardisson, E. Murad, J.D. Fabris, T. Matencio, T.C. Ramalho, M.V.J. Rocha, J. Mater. Chem. 21 (2011) 10280–10282.
[29] T.S. Rocha, E.S. Nascimento, A.C. Silva, H.S. Oliveira, E.M. Garcia, L.C.A. Oliveira, D.S. Monteiro, M. Rodriguez, M.C. Pereira, RSC Adv. 3 (2013) 20308–20314.
[30] W. Du, Y. Xu, Y. Wang, Langmuir 24 (2008) 175–181.
[31] X. Su, F. Xiao, Y. Li, J. Jian, Q. Sun, J. Wang, Mater. Lett. 64 (2010) 1232–1234.
[32] I.S.X. Pinto, P.H.V.V. Pacheco, J.K. Viana, E. Lorençon, J.D. Ardisson, J.D. Fabris, P.P. Souza, K.W.H. Krambrock, L.C.A. Oliveira, M.C. Pereira, Appl. Catal., B—Environ. 119–120 (2012) 175–182.
[33] P. Chagas, A.C. Silva, E.C. Passamani, J.D. Ardisson, L.C.A. Oliveira, J.D. Fabris, R.M. Paniago, D.S. Monteiro, M.C. Pereira, J. Nanopart. Res. 15 (2013) 1–7.
[34] C.B. Koch, C.A. Oxborrow, S. Mørup, M.B. Madsen, A.J. Quinn, J.M.D. Coey, Phys. Chem. Miner. 22 (1995) 333–341.
[35] M.B. Madsen, S. Mørup, Surf. Sci. 156 (1985) 328–334.
[36] M. Gotić, M. Ivanda, S. Popović, S. Musić, Mater. Sci. Eng. B77 (2000) 193–201.
[37] M. Gotić, S. Popović, S. Musić, Mater. Lett. 21 (1994) 289–295.
[38] A. Periasamy, S. Muruganand, M. Palaniswamy, Rasayan J. Chem. 2 (2009) 981–989.
[39] D.L.A. Faria, S.V. Silva, M.T. Oliveira, J. Raman Spectrosc. 28 (1997) 873–878.

[40] R.M. Cornell, U. Schwertmann, The Iron Oxides—Structure, Properties, Reactions, Occurrences and Uses, second ed., Wiley-VCH, Weinheim, 2003.
[41] M.C. Pereira, F.S. Coelho, C.C. Nascentes, J.D. Fabris, M.H. Araújo, K. Sapag, L.C.A. Oliveira, R.M. Lago, Chemosphere 81 (2010) 7–12.
[42] V. Logie, G. Maire, D. Michel, J.L. Vignes, J. Catal. 188 (1999) 90–101.
[43] R.J. Baxter, P. Hu, J. Chem. Phys. 116 (2002) 4379–4381.
[44] W. Li, D. Li, Y. Lin, P. Wang, W. Chen, X. Fu, Y. Shao, J. Phys. Chem. C 116 (2012) 3552–3560.
[45] J. Cao, B. Luo, H. Lin, B. Xu, S. Chen, Appl. Catal. B—Environ. 111–112 (2012) 288–296.
[46] W. Wang, L. Zhang, T. An, G. Li, H.Y. Yip, P.K. Wong, Appl. Catal., B—Environ. 108–109 (2011) 108–116.
[47] C. Tizaoui, N. Karodia, M. Aburowais, J. Chem. Technol. Biotechnol. 85 (2010) 234–242.